

Electronic Supporting Information for:

Dynamic Motion of Organic Spacer Cations in Ruddlesden-Popper Lead Iodide Perovskites Probed by Solid-State NMR Spectroscopy

Clayton J. Dahlman[§], Rhys M. Kennard[§], Piotr Paluch[#], Naveen R. Venkatesan[§]
Michael L. Chabiny^{§*} and G. N. Manjunatha Reddy^{†*}

[§] *Materials Department, University of California, Santa Barbara, California 93106, U. S. A.*

[#] *Centre of Molecular and Macromolecular Studies, Polish Academy of Sciences, Sienkiewicza 112, 90-363 Lodz, Poland*

[†] *Univ. Lille, CNRS, Centrale Lille, Univ. Artois, UMR 8181- UCCS - Unité de Catalyse et Chimie du Solide, F-59000 Lille, France*

**Corresponding authors emails: mchabiny@engineering.ucsb.edu, gnm.reddy@univ-lille.fr*

Table of contents

1. Theory of NMR cross-polarization kinetics
2. X-ray diffraction patterns of RP phases
3. Unit cells and space groups of RP phases
4. 2D ¹H{¹³C} heteronuclear correlation NMR spectra of RP phases
5. 2D ¹H{¹H} DQ-SQ correlation NMR spectra of {C8} RP phase
6. 1D ¹³C{¹H} CP-MAS NMR spectra of {C4} precursor salt and RP phase
7. 1D ¹³C{¹H} CP-MAS NMR spectra of {C8} precursor salt and RP phase
8. 1D ¹³C{¹H} CP-MAS NMR spectra of {C12} precursor salt and RP phase
9. ¹³C{¹H} CP build up curves of alkylammonium precursor salts
10. 1D ¹³C{¹H} CP-MAS NMR spectra of {PhC2} precursor salt and RP phase
11. 1D ¹H MAS NMR spectra of {PhC2} RP phase and precursor salt, and 2D ¹H{¹H} DQ-SQ correlation NMR spectrum of {PhC2} RP phase.
12. 1D ¹⁵N{¹H} CP-MAS NMR spectra of precursor salt and RP phase for each spacer

1. Theory of NMR cross-polarization kinetics

CP-MAS ssNMR experiment. The quantitative treatment of cross polarization (CP) intensity build-up under the magic-angle spinning (MAS) condition is complex and depends on compositions, structures and several kinetic processes.^{1,2} The site-specific dynamic motion examined by CP signal intensity build-up refers to local fluctuations in the arrangements of spin-polarized atoms. For example, in non-paramagnetic materials fluctuations in relative nuclear positions occur with a characteristic time scale described by molecular reorientation ‘correlation times’, τ_c . In soft materials, the time required for CP build-up is found to scale linearly with τ_c .¹ Molecular reorientation is thermally activated, so the correlation time is commonly described by Arrhenius kinetics:

$$\tau_c = \tau_0 \exp(E_a/kT) \quad \text{Equation S1}$$

Here, τ_0 is the correlation time at 0 K, E_a is the activation energy, k is the Boltzmann constant and T is the temperature. A thermal gradient (i.e., variable temperature NMR experiments) is often used to relate CP-MAS build-up kinetics to reorientation correlation times, τ_c .³ However, many RP spacer molecules undergo thermal structural transformations that can obscure these measurements. Fortunately, molecular reorientation impacts many different relaxation and exchange processes in NMR experiments, including CP signal intensity build-up,^{1,2,4} which can be used to relate CP-MAS build-up kinetics to molecular correlation times. For instance, temperature-dependent studies of line-broadening through T_2 or $T_{1,\rho}$ relaxation have been used to study $\{\text{PhC}_2\}_2\text{PbI}_4$ spacer dynamics,^{5,6} and provide a benchmark for CP build-up kinetics. Within these limits, relative trends in correlation times can be compared if the molecular environment and relaxation rates are similar.

By carrying out 1D CP-MAS experiments with increasing CP contact time, the CP signal intensity buildup can be measured and analyzed at a single temperature (**Figure 3**). The relationship between signal intensity at a given CP contact time, $I(t)$, and the maximum intensity, I_0 , can be approximated as,⁷

$$I(t) = I_0(1 - \exp\{-k_{CP}t\}) \quad \text{Equation S2}$$

Here, k_{CP} is the CP rate constant, which depends strongly on dipole interactions between the abundant nuclei (^1H) and the scarce nuclei, X (i.e. ^{13}C or ^{15}N), which in turn relate to the densities of hydrogen atoms in the vicinity of $^{13}\text{C}/^{15}\text{N}$ nuclei and local molecular motions. This model assumes that nuclear spins do not relax over the timescale of the CP-MAS experiment (i.e. $1/k_{CP} \ll T_{1,\text{H}}, T_{1,\text{X}}$). Fast X $\{^1\text{H}\}$ CP buildup is thus expected in rigid systems containing many hydrogen atoms in the immediate vicinity (within ~ 1 nm) of X nuclei. Directly-bonded hydrogens are the primary source of CP magnetization in these species at short CP contact times (< 0.1 ms), whereas the adjacent hydrogen atoms in close proximities (< 1 nm) likely contribute to CP intensity build up at longer CP contact times (> 0.1 ms).

Variations and disorder in local dynamics significantly influence the CP signal intensity build up, leading to deviations in the exponential kinetics. Such variations may be empirically modelled by incorporating a correction factor b into the exponential term of **Equation S2**.⁷ Further complication may arise when the homonuclear relaxation of abundant ^1H nuclei, $k_{1,\text{H}}$, is fast enough to compete with CP kinetics, and an additional exponential decay must be accounted for:

$$I(t) = I_0(1 - k_{1,H}/k_{CP})^{-1}(\exp\{-k_{1,H}t\} - \exp\{-k_{CP}t\}^b) \quad \text{Equation S3}$$

Each resolvable signal intensity associated with a chemically inequivalent site in a CP NMR experiment can be fit to distinct CP build-up kinetics using **Equation S3**. From the curve fitting analyses, the CP rate constant (k_{CP}) and time constants ($T_{CP} = 1/k_{CP}$) can be derived and compared for the rigid and flexible sites. A comparison of these CP build-up kinetics can provide site-specific information about the motional dynamics of spacer molecules that can be benchmarked to other studies of absolute molecular correlation times, τ_c .

CP-Variable Contact (CP-VC) Experiment. The $^1\text{H} \rightarrow ^{13}\text{C}$ CP magnetization transfer, under MAS, can be achieved via the Hartmann–Hahn-sideband condition either in a zero-quantum (ZQ) or in a double-quantum (DQ) pathway. While the Hartmann–Hahn condition for the ZQ-CP experiment generally requires that the difference of the radio frequency (RF) amplitudes of ^1H and ^{13}C to be synchronized with the MAS frequency, the DQ-CP condition requires that the sum of the RF-amplitudes to be synchronized with the MAS frequency.³ Likewise, the CP-VC experiments use the sum or the difference of RF-fields equal to the spinning rate as it reintroduces the maximum of dipolar interactions. Fitting of these dipolar oscillations, and subsequently the Fourier transformation leads to a separation of frequencies in the vertical dimension of a 2D CP-VC experiment.^{8–10}

Dipolar-mediated 2D $^{13}\text{C}\{^1\text{H}\}$ CP-VC experiments correlate ^{13}C chemical shifts with C-H dipole-dipole couplings, D_{CH} . The frequency separation between the signals in the indirect vertical dimension of CP-VC spectra scales with the motion of different C-H dipole-dipole couplings. For example, a doublet is often observed in powdered samples with a frequency separation, $\Delta = D_{\text{CH}}/\sqrt{2}$, where D_{CH} is the C-H dipole-dipole coupling in kHz. In the absence of molecular motions, the dipolar-interaction tensor is axially symmetric with components $-D_{\text{CH}}/2$ and $D_{\text{CH}}/2$, which corresponds to the theoretical maximum of ^{13}C - ^1H dipolar coupling, $D_{\text{CH}} = 23$ kHz. When the C-H bond undergoes fast reorientation, the axial symmetry of the dipolar tensor splits into principal components D_{xx} , D_{yy} , D_{zz} , and reduces the magnitude of the effective dipolar tensor.^{3,11} Thus, molecular reorientation can be probed by comparing CP-VC dipolar splittings to the limits of a perfectly rigid molecule ($D_{\text{CH,max}} \approx 23$ kHz) or a rapidly re-orienting molecule within the μs timescale of the ssNMR experiment.

2. X-ray diffraction patterns of RP phases

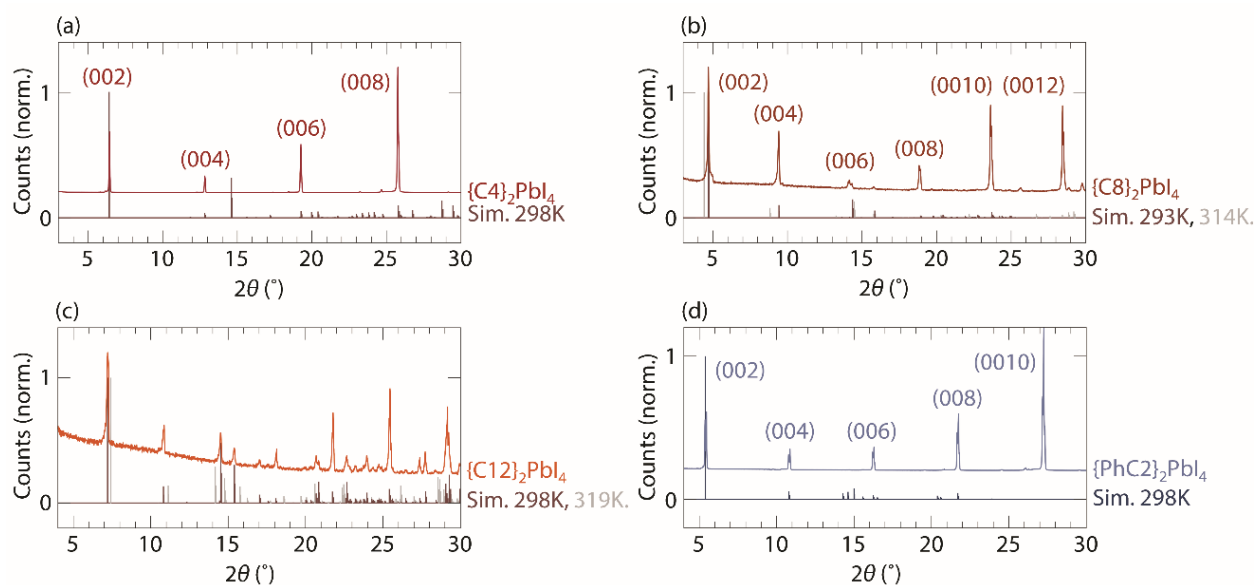


Figure S1. Powder X-Ray diffraction (XRD) patterns overlaid with powder simulations for (a) $\{C4\}_2PbI_4$, (b) $\{C8\}_2PbI_4$, (c) $\{C12\}_2PbI_4$ and (d) $\{PhC2\}_2PbI_4$. Simulated patterns were taken from published single-crystal XRD refinements.^{12–15} Simulated patterns were plotted for both the room temperature phase and the higher-temperature phase for (b) $\{C8\}_2PbI_4$ and (c) $\{C12\}_2PbI_4$, due to the proximity of phase transitions near 314K and 319K respectively. Single crystals were measured for (a), (b), and (d); the patterns thus exhibit the preferred orientation of the crystal. For (c), the compound was roughly ground. Occasional peak splitting was observed due to detector saturation, as the compounds diffracted quite strongly.

3. Unit cells and space groups of RP phases

(a) $n = 1$ Ruddlesden-Popper phases at 293 K

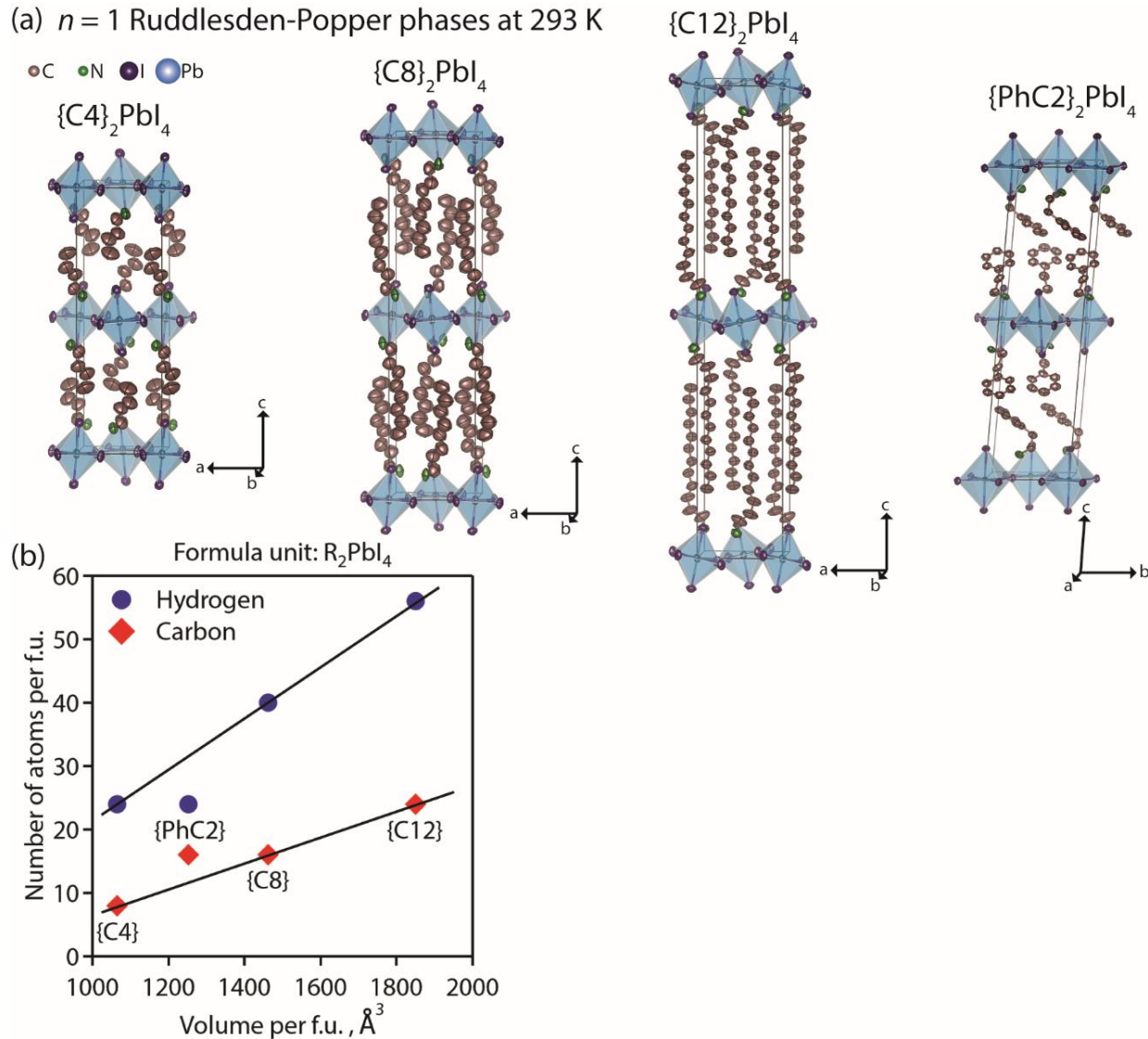


Figure S2. a) Unit cells derived from previously reported single-crystal X-ray diffraction refinements of each of the RP phases described in the text: orthorhombic $Pbca$ RP phases with n -butylammonium $\{C4\}$ spacers,¹⁴ n -octylammonium $\{C8\}$ spacers,¹² and n -dodecylammonium $\{C12\}$ spacers,¹³ and monoclinic $P\bar{1}$ with phenethylammonium $\{PhC2\}$ spacers.¹⁵ Anisotropic thermal ellipsoids are shown for 60% occupation probability with the same length scaling across all unit cells. The hydrogen atoms were not refined in any of the published phases, and are omitted. Portions of the unit cells were omitted (half of the unit cell along b for $\{C4\}$, $\{C8\}$ and $\{C12\}$ phases, and half of the unit cell along a for the $\{PhC2\}$ phase) to avoid overlap between spacers for visual clarity. b) A comparison of C and H atom quantities to formula unit cell volume for RP phases. Assuming a similar octahedral volume for all samples, $\{PhC2\}_2PbI_4$ has a slightly lower density of H atoms, and higher density of C atoms, in the interlayer than the linear spacers.

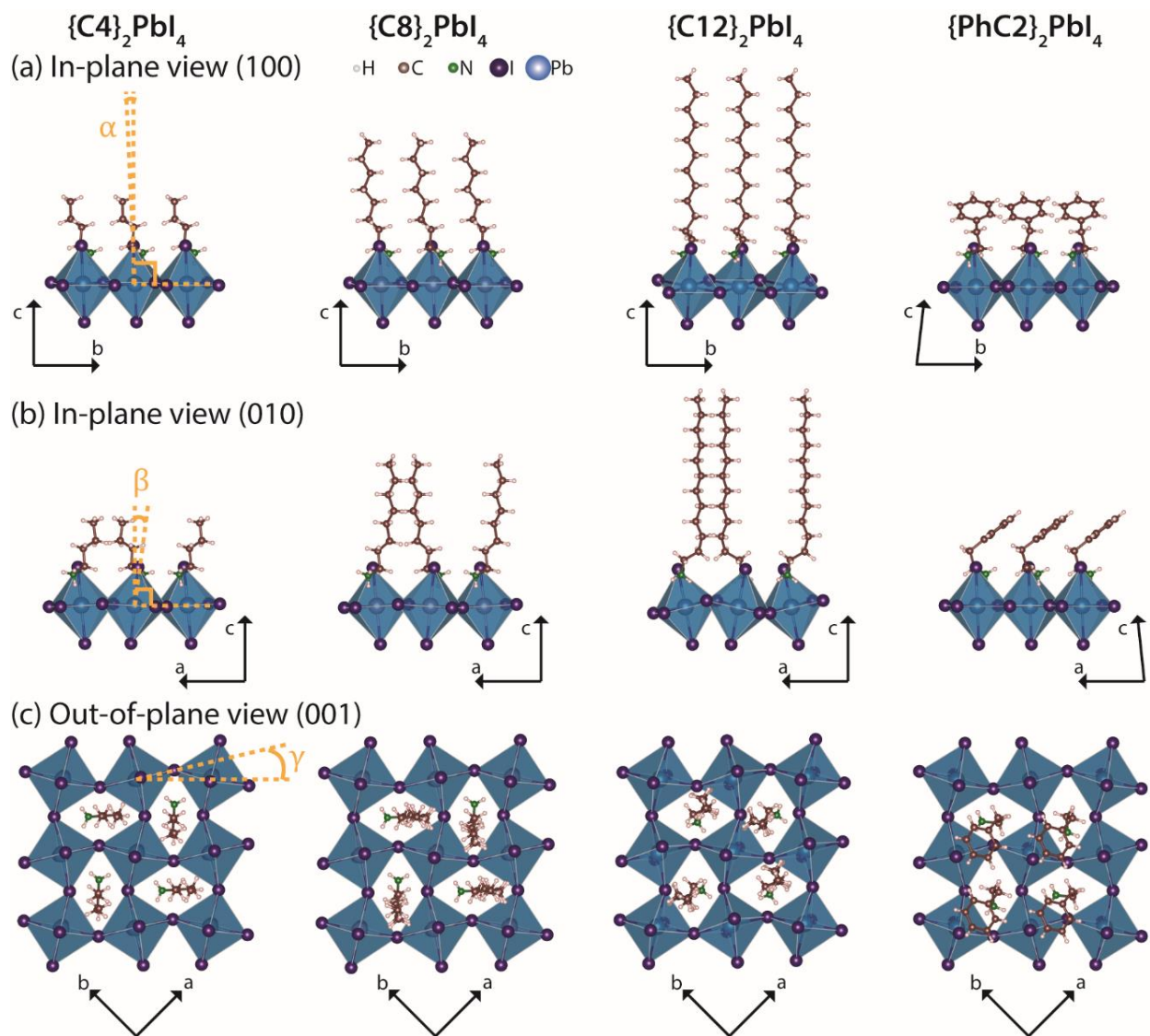


Figure S3. Crystal structures derived from previously reported single-crystal X-ray diffraction refinements of RP phases at room temperature, showing octahedral tilting for orthorhombic $Pbca$ phases with *n*-butylammonium $\{C4\}$ spacers,¹⁴ *n*-octylammonium $\{C8\}$ spacers,¹² and *n*-dodecylammonium $\{C12\}$ spacers,¹³ and monoclinic $P\bar{1}$ with phenethylammonium $\{PhC2\}$ spacers.¹⁵ In-plane views of the a) (100) plane and b) (010) plane show apical tilting about *a* and *b*, respectively.) An out-of-plane view of the (001) plane shows axial tilting about *c*. Angles of tilting are defined for each projection, and tabulated in **Table S1**.

Table S1. Unit cell properties obtained from single-crystal XRD refinements for each of the RP phases illustrated in **Figures S2** and **S3**. The tilt systems are defined based on the conventions outlined in Aleksandrov et al. for $n = 1$ RP phases.^{16,17} An analogous tilt system label is also defined, using the Glazer notation for perovskite tilting.¹⁸ Two angles are given for tilt about c (*i.e.* the (001) plane) because octahedral distortions produce two axial tilt angles in the refined structures. The octahedral penetration was measured as the distance between the plane connecting the apical iodides and the spacer N atom.

	{C4}₂PbI₄	{C8}₂PbI₄	{C12}₂PbI₄	{PhC2}₂PbI₄
Space group	<i>Pbca</i>	<i>Pbca</i>	<i>Pbca</i>	<i>P-1</i>
Aleksandrov tilt system	$\Phi_1\Phi_2\Psi_z$	$\Phi_1\Phi_2\Psi_z$	$\Phi_1\Phi_2\Psi_z$	$\Phi_1\Phi_2\Psi_z$
Pseudo-Glazer tilt system	$a^-b^-c^+$	$a^-b^-c^+$	$a^-b^-c^+$	$a^-b^-c^+$
α (about a)	2.4°	2.5°	3.1°	2.8°
β (about b)	5.5°	5.5°	10.5°	2.1°
γ (about c)	12.5°, 13.0°	10.5°, 12.5°	10.5°, 12.5°	13°
Closest N-I distance	3.598 Å	3.610 Å	3.592 Å	3.666 Å
Octahedral penetration	0.5893 Å	0.6233 Å	0.4719 Å	0.5526 Å

4. 2D $^1\text{H}\{^{13}\text{C}\}$ heteronuclear correlation NMR spectra of RP phases

In alkylammonium spacer cations, the local bonding environments of CH, CH₂ and CH₃ groups are distinguishable by analyzing 2D ^{13}C - ^1H correlation intensities: for example, 2D correlation peaks between ^{13}C (15-20 ppm) and ^1H (1.1 ppm) are attributed to terminal methyl groups, and a distribution of correlation intensities between ^{13}C (20-40 ppm) and ^1H (1.5-2.5 ppm) signals are observed for central methylene groups, with a greater diversity of features observed for the longer spacers. Well-resolved 2D correlation intensities between ^{13}C signals at 40-45 ppm and ^1H signals at 3-4 ppm correspond to methylene groups adjacent to NH_3^+ groups. The number and chemical shifts of correlated peaks differ between $\{\text{C}4\}_2\text{PbI}_4$, $\{\text{C}8\}_2\text{PbI}_4$ and $\{\text{C}12\}_2\text{PbI}_4$, but the results allow for direct assignments of ^1H and ^{13}C chemical shifts to particular sites in each spacer, as tabulated in **Tables S2-S5**. For $\{\text{PhC}2\}_2\text{PbI}_4$, the 2D correlation intensities between the ^{13}C signals at 36 and 45 ppm and ^1H signals between 2.5-4.5 ppm are ascribed to CH₂ groups, while the ^{13}C signals originate from different C-H moieties in phenyl groups in the range 120-140 ppm correlate with the ^1H signals between 6-8 ppm.

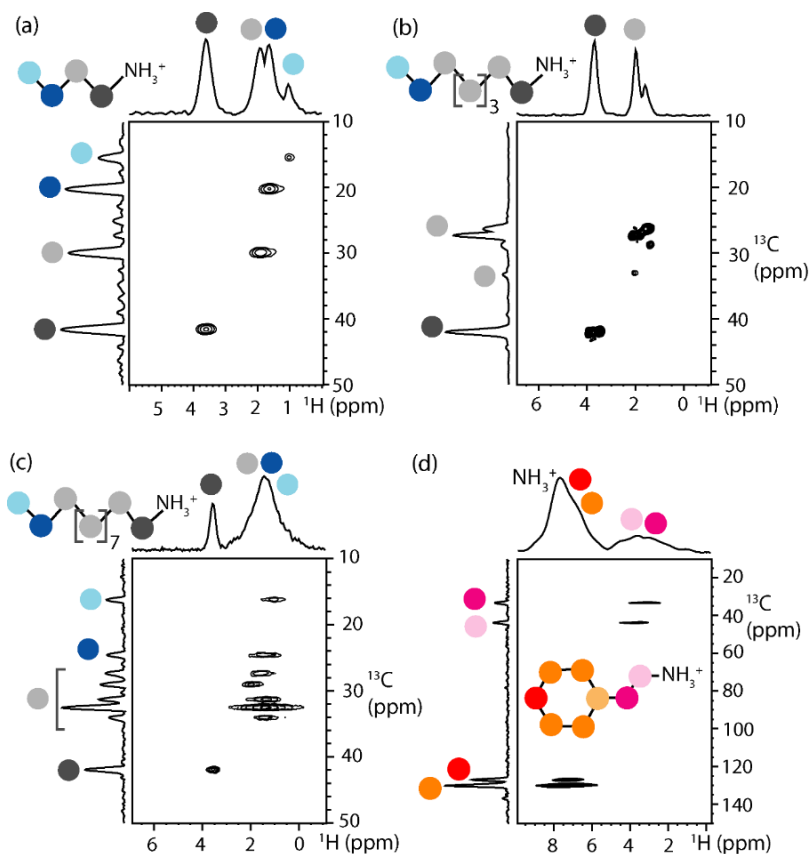


Figure S4. Solid-state 2D $^1\text{H}\{^{13}\text{C}\}$ heteronuclear correlation (HETCOR) NMR correlation spectra acquired at 18.8 T and at 50 kHz MAS of (a) $\{\text{C}4\}_2\text{PbI}_4$, (b) $\{\text{C}8\}_2\text{PbI}_4$, (c) $\{\text{C}12\}_2\text{PbI}_4$, and (d) $\{\text{PhC}2\}_2\text{PbI}_4$ RP ($n = 1$) phases. The ^{13}C dimension was acquired using indirect detection via ^1H dimension. The corresponding skyline projections are shown along the top ^1H horizontal and ^{13}C vertical axes, respectively. Correlated signal intensity originates from dipolar-coupled ^1H - ^{13}C pairs are depicted by colored circles. Increased local mobilities of end groups diminish the 2D HETCOR signals, which may account for the lack of signals from terminal CH₃ (light blue) and CH₂ (dark blue) sites in $\{\text{C}8\}_2\text{PbI}_4$ (**Figure S4b**), which is also corroborated by narrow ^1H signals.

5. 2D $^1\text{H}\{^1\text{H}\}$ DQ-SQ correlation NMR spectra of {C8} RP phase

In the 2D ^1H DQ-SQ NMR spectrum of $\{\text{C8}\}_2\text{PbI}_4$ (**Figure S5**), self-correlation ^1H DQ intensities at $1.1 + 1.1 = 2.1$ ppm, $1.4 + 1.4 = 2.8$ ppm, $2.0 + 2.0 = 4.0$ ppm, $3.8 + 3.8 = 7.6$ ppm, and $7.1 + 7.1 = 14.2$ ppm correspond to CH_3CH_2 (light blue), CH_2 (dark blue), CH_2 (light gray), CH_2 (dark gray) and NH_3^+ groups, respectively, as depicted in the schematic structure. In addition, the cross-correlated ^1H DQ intensity at $1.4 + 3.8 = 5.2$ ppm is attributed to the protons in the adjacent CH_2 and CH_2 groups within the same $\{\text{C8}\}$ cation. In addition, the ^1H DQ signals at $1.4 + 7.1 = 8.5$ ppm, $2.0 + 7.1 = 9.1$ ppm and at $3.8 + 7.1 = 11.9$ ppm correspond to $\text{NH}_3\text{-CH}_2$ (light gray), $\text{NH}_3\text{-CH}_2$ (light gray) and $\text{NH}_3\text{-CH}_2$ (dark blue) are distinguished and identified. These cross-correlated ^1H DQ intensities suggest the close spatial proximities between $\text{CH}_3\text{-CH}_2$, $\text{CH}_2\text{-CH}_2$, and $\text{NH}_3\text{-CH}_2$ groups of the $\{\text{C8}\}$ spacer cations in the RP phase, $\{\text{C8}\}_2\text{PbI}_4$.

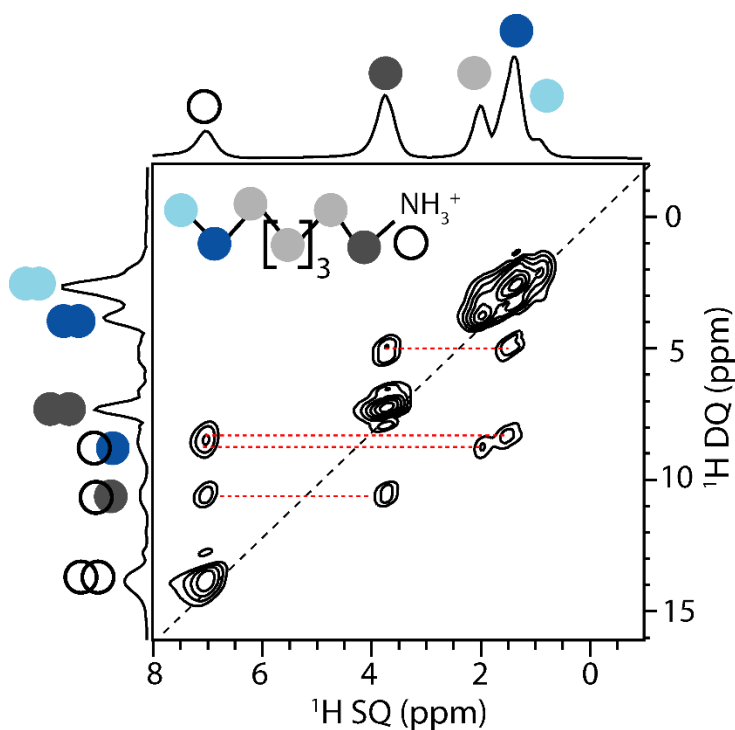


Figure S5. Solid-state 2D $^1\text{H}\{^1\text{H}\}$ DQ-SQ NMR correlation spectrum of $\{\text{C8}\}_2\text{PbI}_4$ acquired at 18.8 T (^1H 800.1 MHz) and at 50 kHz MAS frequency. The corresponding skyline projections are shown along the top ^1H SQ horizontal and ^1H DQ vertical axes, respectively. Correlated signal intensity originates from dipolar-coupled $^1\text{H}\text{-}^1\text{H}$ pairs are depicted by colored circles.

6. 1D $^{13}\text{C}\{^1\text{H}\}$ CP-MAS NMR spectra of {C4} precursor salt and RP phase

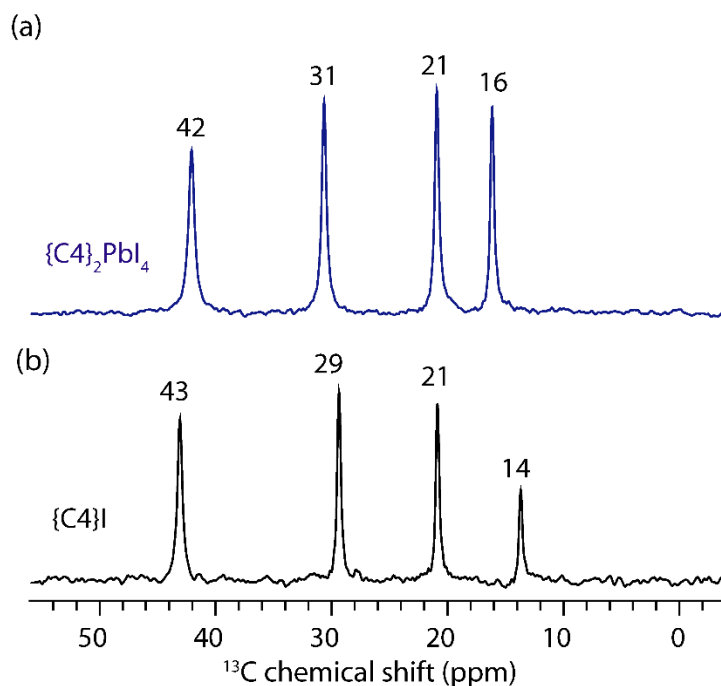


Figure S6. Solid-state 1D $^{13}\text{C}\{^1\text{H}\}$ CP-MAS NMR spectra of (a) $\{\text{C4}\}_2\text{PbI}_4$ and (b) $\{\text{C4}\}\text{I}$.

Table S2. Signal intensity buildup fitting parameters and CP rate constants associated with different $^{13}\text{C}\{^1\text{H}\}$ and $^{15}\text{N}\{^1\text{H}\}$ signals of $\{\text{C4}\}_2\text{PbI}_4$ and $\{\text{C4}\}\text{I}$.

$\{\text{C4}\}_2\text{PbI}_4$	Chemical shift (ppm)	k_{CP} (ms^{-1})	b
C-1	42	23.47 ± 1.84	0.51 ± 0.03
C-2	31	6.32 ± 0.27	0.58 ± 0.03
C-3	21	3.62 ± 0.14	0.54 ± 0.02
C-4	16	0.77 ± 0.03	1.00 ± 0.05
N	-331	0.41 ± 0.01	0.89 ± 0.03

$\{\text{C4}\}\text{I}$	Chemical shift (ppm)	k_{CP} (ms^{-1})	b
C-1	43	1.03 ± 0.12	0.57 ± 0.06
C-2	29	0.99 ± 0.10	0.60 ± 0.06
C-3	21	1.03 ± 0.07	0.68 ± 0.05
C-4	14	0.60 ± 0.03	1.00 ± 0.06
N	-331	0.25 ± 0.02	0.97 ± 0.11

7. 1D $^{13}\text{C}\{^1\text{H}\}$ CP-MAS NMR spectra of {C8} precursor salt and RP phase

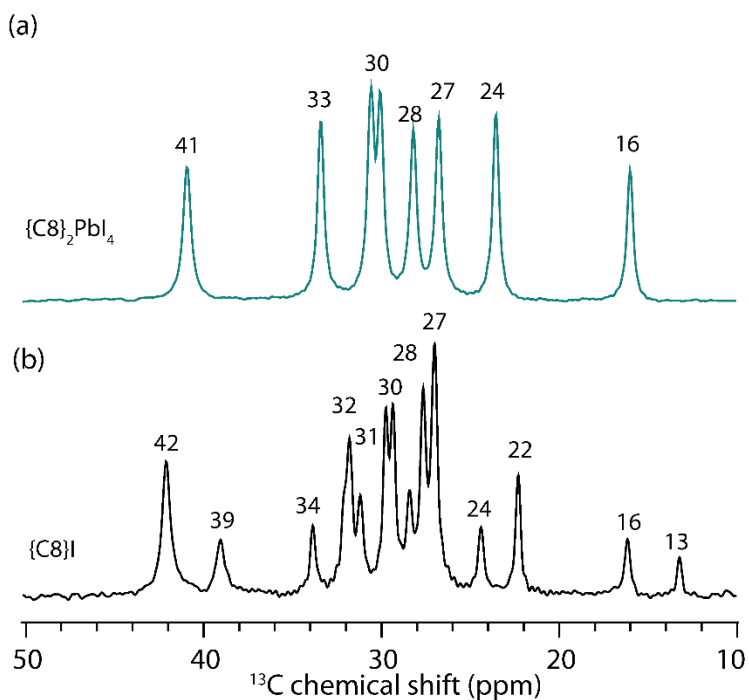


Figure S7. Solid-state 1D $^{13}\text{C}\{^1\text{H}\}$ CP-MAS NMR spectra of (a) $\{\text{C8}\}_2\text{PbI}_4$ and (b) $\{\text{C8}\}\text{I}$, acquired at 9.4 T and at 8 kHz MAS frequency.

Table S3. Signal intensity buildup fitting parameters and CP rate constants associated with different $^{13}\text{C}\{^1\text{H}\}$ and $^{15}\text{N}\{^1\text{H}\}$ signals of $\{\text{C8}\}_2\text{PbI}_4$ and $\{\text{C8}\}\text{I}$. For CP build-up of the ammonium N site in $\{\text{C8}\}_2\text{PbI}_4$, the fitted ^1H homonuclear relaxation rate, $k_{1,H}$, is $0.012 \pm 0.01 \text{ ms}^{-1}$ (**Equation S3**). $\{\text{C8}\}\text{I}$ shows the ^{13}C signals originating from both *trans* and *gauche* conformations, as discussed in the main text about the gamma-gauche effect, so there are more peaks in the $^{13}\text{C}\{^1\text{H}\}$ 1D NMR spectrum (**Figure S7b**) than listed in the table. The values shown in the table below indicate the chemical shifts used for measuring CP build-up kinetics.

$\{\text{C8}\}_2\text{PbI}_4$	Chemical shift (ppm)	$k_{CP} (\text{ms}^{-1})$	b
C-1	41	1.10 ± 0.14	0.52 ± 0.06
C-2	33	0.62 ± 0.08	0.71 ± 0.10
C-3	31	0.70 ± 0.08	0.69 ± 0.08
C-4	30	0.70 ± 0.08	0.69 ± 0.08
C-5	28	0.87 ± 0.14	0.53 ± 0.08
C-6	27	0.79 ± 0.13	0.55 ± 0.08
C-7	24	0.61 ± 0.10	0.64 ± 0.10
C-8	16	0.54 ± 0.14	0.55 ± 0.13
N	-330	1.04 ± 0.11	1.00 ± 0.15

$\{\text{C8}\}\text{I}$	Chemical shift (ppm)	$k_{CP} (\text{ms}^{-1})$	b
C-1	42	2.37 ± 0.29	0.42 ± 0.04
C-2	34	2.40 ± 0.27	0.43 ± 0.04
C-3	31	0.85 ± 0.11	0.59 ± 0.07
C-4	30	1.39 ± 0.19	0.50 ± 0.06
C-5	28	1.39 ± 0.19	0.50 ± 0.06
C-6	27	0.73 ± 0.11	0.59 ± 0.08
C-7	24	0.64 ± 0.10	0.63 ± 0.10
C-8	16	0.50 ± 0.05	0.87 ± 0.11
N	-330	0.74 ± 0.03	0.83 ± 0.04

8. 1D $^{13}\text{C}\{^1\text{H}\}$ CP-MAS NMR spectra of {C12} precursor salt and RP phase

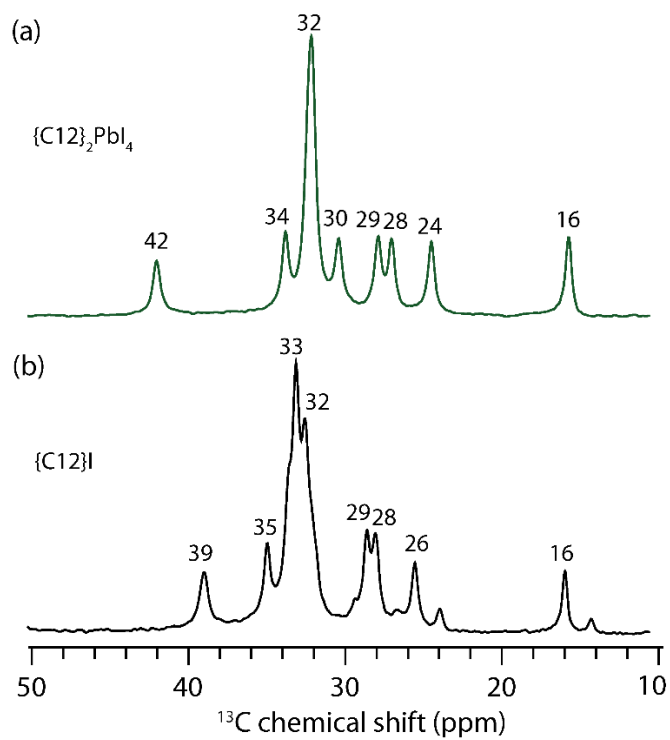


Figure S8. Solid-state 1D $^{13}\text{C}\{^1\text{H}\}$ CP-MAS NMR spectra of (a) $\{\text{C12}\}_2\text{PbI}_4$ and (b) $\{\text{C12}\}\text{I}$.

Table S4. Signal intensity buildup fitting parameters and CP rate constants associated with different $^{13}\text{C}\{^1\text{H}\}$ and $^{15}\text{N}\{^1\text{H}\}$ signals of $\{\text{C12}\}_2\text{PbI}_4$ and $\{\text{C12}\}\text{I}$. For CP build-up of the ammonium N site in $\{\text{C12}\}_2\text{PbI}_4$, the fitted ^1H homonuclear relaxation rate, $k_{I,H}$, is $0.012 \pm 0.004 \text{ ms}^{-1}$ (**Equation S3**). $\{\text{C12}\}\text{I}$ exhibits signals correspond to both *trans* and *gauche* conformations, as discussed in the main text about the gamma-gauche effect, and there are the low intensity and low frequency peaks in the $^{13}\text{C}\{^1\text{H}\}$ 1D NMR spectrum (**Figure S8b**). The values shown in the table below indicate the chemical shifts used for measuring CP build-up kinetics.

$\{\text{C12}\}_2\text{PbI}_4$	Chemical shift (ppm)	$k_{CP} (\text{ms}^{-1})$	b
C-1	42	0.85 ± 0.17	0.50 ± 0.09
C-2	34	1.69 ± 0.25	0.47 ± 0.06
C-3-7	32	1.97 ± 0.20	0.50 ± 0.04
C-8	30	1.88 ± 0.21	0.47 ± 0.05
C-9	28	1.88 ± 0.21	0.47 ± 0.05
C-10	24	1.76 ± 0.15	0.51 ± 0.04
C-11	27	1.40 ± 0.24	0.43 ± 0.06
C-12	16	0.67 ± 0.09	0.66 ± 0.09
N	-333	1.38 ± 0.09	1.00 ± 0.10

$\{\text{C12}\}\text{I}$	Chemical shift (ppm)	$k_{CP} (\text{ms}^{-1})$	b
C-1	39	3.35 ± 0.19	0.49 ± 0.03
C-2	35	4.57 ± 0.28	0.48 ± 0.03
C-3-7	33	3.80 ± 0.27	0.62 ± 0.05
C-8	32	3.80 ± 0.27	0.62 ± 0.05
C-9	29	3.65 ± 0.23	0.59 ± 0.04
C-10	28	3.05 ± 0.12	0.61 ± 0.03
C-11	26	3.17 ± 0.36	0.57 ± 0.07
C-12	16	1.25 ± 0.09	0.67 ± 0.05
N	-327	1.33 ± 0.03	0.99 ± 0.03

9. $^{13}\text{C}\{^1\text{H}\}$ CP build up curves of alkylammonium precursor salts

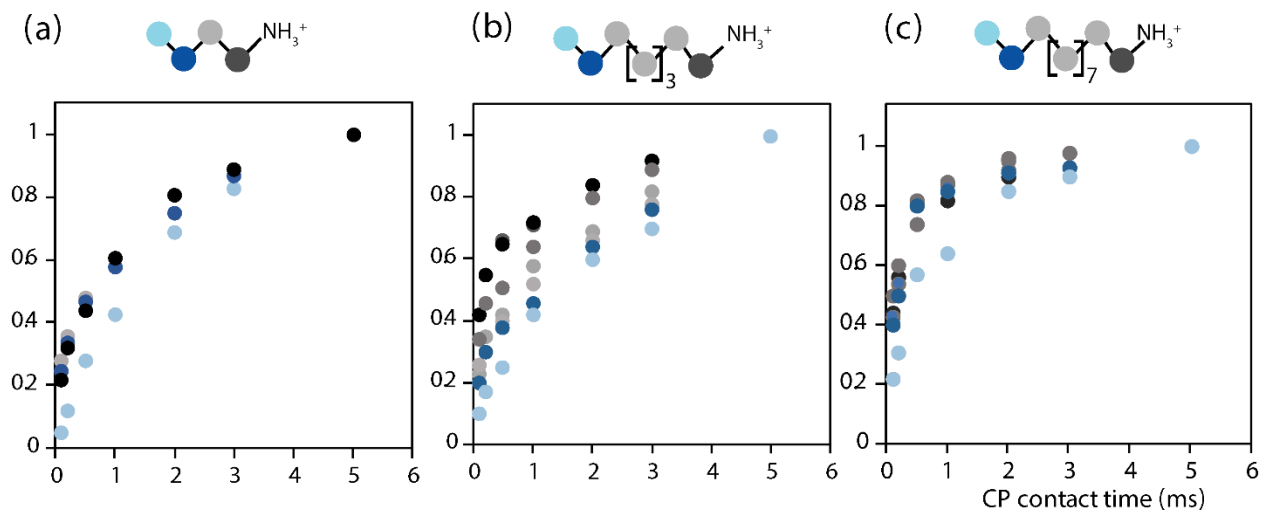


Figure S9. $^{13}\text{C}\{^1\text{H}\}$ CP signal intensity build-up curves associated with different ^{13}C sites in ammonium iodide salts (a) $\{\text{C4}\}\text{I}$, (b) $\{\text{C8}\}\text{I}$ and (c) $\{\text{C12}\}\text{I}$, as functions of CP contact times. The signal intensities are normalized with respect to the $^{13}\text{C}\{^1\text{H}\}$ highest signal intensity for each site.

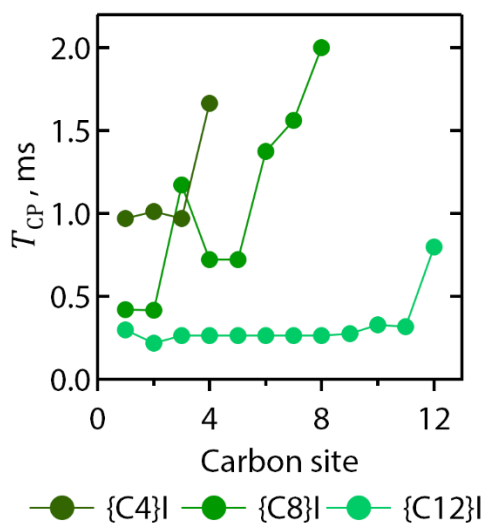


Figure S10. Site-specific CP build-up parameters T_{cp} ($= 1/k_{cp}$) for each carbon in alkylammonium iodide salts.

10. 1D $^{13}\text{C}\{^1\text{H}\}$ CP-MAS spectra of $\{\text{PhC2}\}$ precursor salt and RP phase

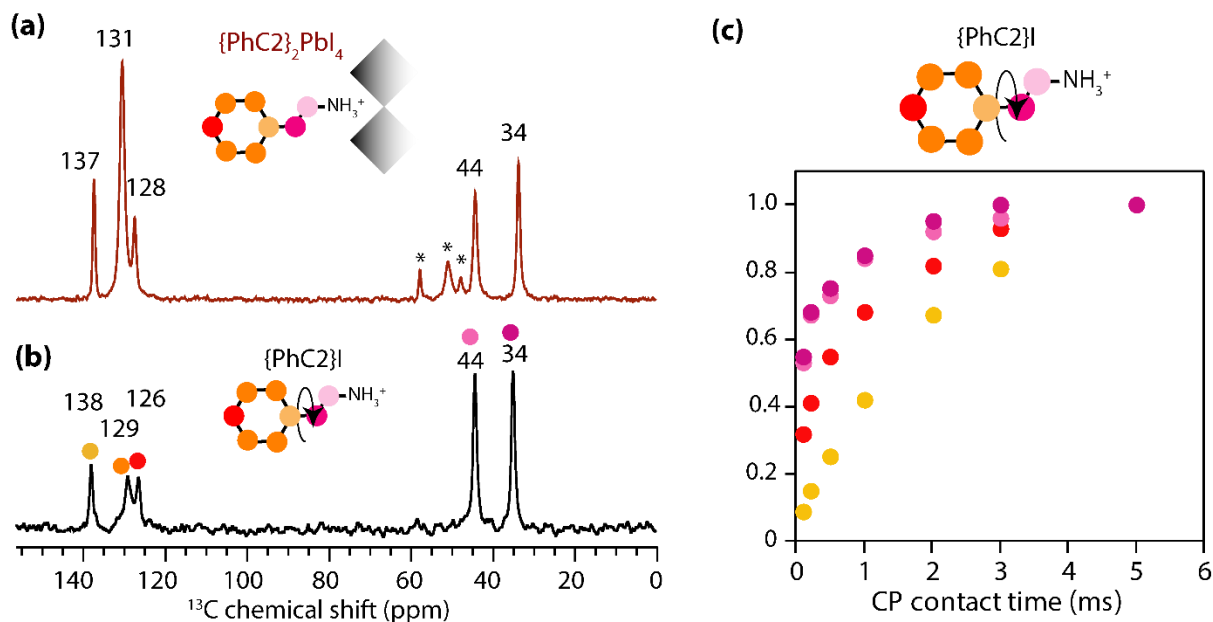


Figure S11. Solid-state 1D $^{13}\text{C}\{^1\text{H}\}$ CP-MAS NMR spectra of (a) $\{\text{PhC2}\}_2\text{PbI}_4$ and (b) $\{\text{PhC2}\}\text{I}$. The ^{13}C signals corresponding to different ^{13}C sites are depicted by colored circles. (c) $^{13}\text{C}\{^1\text{H}\}$ CP signal intensity build-up curves associated with different ^{13}C sites in $\{\text{PhC2}\}\text{I}$. The peaks marked by an asterisk (*) correspond to spinning side-bands.

Table S5. Signal intensity buildup fitting parameters and CP rate constants associated with different $^{13}\text{C}\{^1\text{H}\}$ and $^{15}\text{N}\{^1\text{H}\}$ signals of $\{\text{PhC2}\}_2\text{PbI}_4$ and $\{\text{PhC2}\}\text{I}$.

$\{\text{PhC2}\}_2\text{PbI}_4$	Chemical shift (ppm)	k_{CP} (ms^{-1})	b
C-1	44	8.61 ± 0.90	0.38 ± 0.03
C-2	34	8.45 ± 0.71	0.36 ± 0.02
C-p1	137	1.03 ± 0.09	0.62 ± 0.05
C-p2/3	131	5.12 ± 0.52	0.54 ± 0.06
C-p4	128	5.78 ± 1.01	0.37 ± 0.05
N	-335	0.41 ± 0.03	0.86 ± 0.08

$\{\text{PhC2}\}\text{I}$	Chemical shift (ppm)	k_{CP} (ms^{-1})	b
C-1	44	5.13 ± 0.55	0.39 ± 0.03
C-2	34	5.74 ± 0.71	0.42 ± 0.04
C-p1	138	0.58 ± 0.03	0.98 ± 0.07
C-p2/3	129	1.62 ± 0.10	0.58 ± 0.03
C-p4	126	1.48 ± 0.12	0.55 ± 0.04
N	-330	0.41 ± 0.01	0.89 ± 0.03

Table S6. List of $U_{isotropic}$ parameters obtained from published single-crystal X-ray diffraction refinements of $\{\text{PhC}_2\}_2\text{PbI}_4$ at 298 K.¹⁵

$\{\text{PhC}_2\}_2\text{PbI}_4$	Chemical shift (ppm)	$U_{isotropic}$ (\AA^2)
C-1	45	0.0568
C-2	36	0.0675
C- <i>p</i> 1	139	0.0717
C- <i>p</i> 2/3	130	0.0679
C- <i>p</i> 4	127	0.0653

11.1D ^1H MAS NMR spectra of $\{\text{PhC2}\}$ RP phase and precursor salt, and 2D $^1\text{H}\{^1\text{H}\}$ DQ-SQ correlation spectrum of $\{\text{PhC2}\}$ RP phase.

The 2D ^1H DQ-SQ NMR spectrum of $\{\text{PhC2}\}_2\text{PbI}_4$ is shown below in **Figure S12c**. A broad distribution of self-correlation ^1H DQ intensities at $3.5 + 3.5 = 7.0$ ppm are attributed to spatially proximate CH_2 groups (pink and magenta), and ^1H DQ intensities at $7.0 + 7.0 = 14$ ppm, $7.5 + 7.5 = 15$ ppm, correspond to special proximities between aromatic protons (red, orange) and between protons in NH_3^+ groups, respectively. The cross-correlated ^1H DQ intensities at $3.5 + 7.0 = 10.5$ ppm, and at $3.5 + 7.5 = 11$ ppm originate from the close proximities between the protons in CH_2 (pink, magenta) and aromatic (red, orange) or NH_3^+ groups.

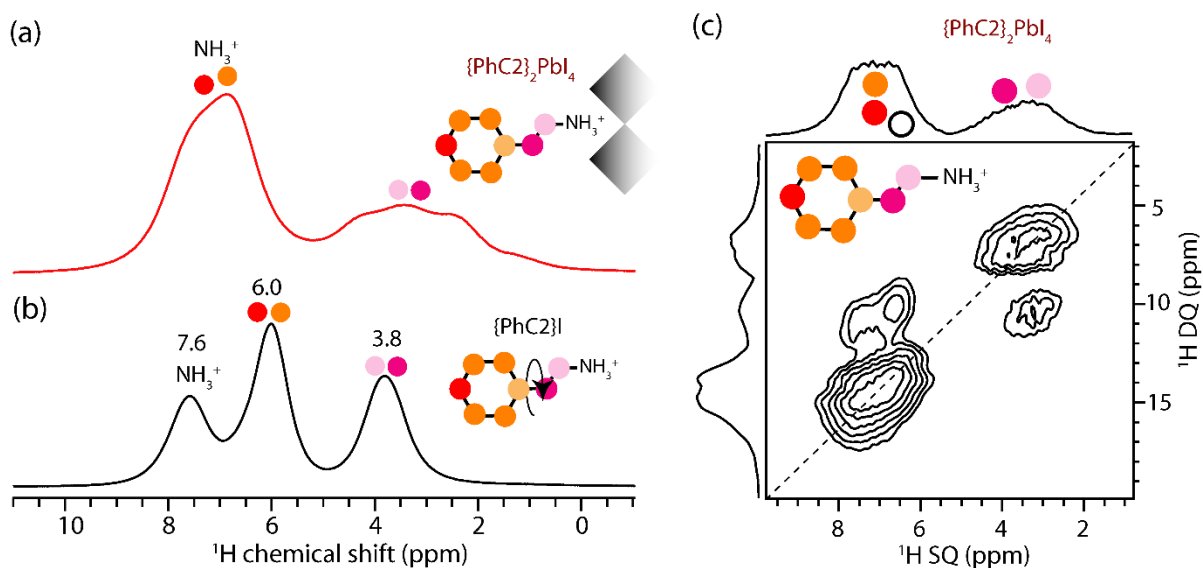


Figure S12. Comparison of solid-state 1D ^1H MAS NMR spectra of (a) $\{\text{PhC2}\}_2\text{PbI}_4$ and (b) $\{\text{PhC2}\}\text{I}$, acquired at 14.1 T (50 kHz MAS). The ^1H signals correspond to different ^1H sites are depicted in colored circles. (c) Solid-state 2D $^1\text{H}\{^1\text{H}\}$ DQ-SQ NMR correlation spectra acquired at 18.8 T and at 50 kHz of $\{\text{PhC2}\}_2\text{PbI}_4$ RP ($n = 1$) phase. The corresponding skyline projections are shown along the top ^1H SQ horizontal and ^1H DQ vertical axes, respectively. Correlated signal intensity originates from dipolar-coupled ^1H - ^1H pairs are depicted by colored circles.

12.1D $^{15}\text{N}\{^1\text{H}\}$ CP-MAS NMR spectra of precursor salt and RP phase for each spacer

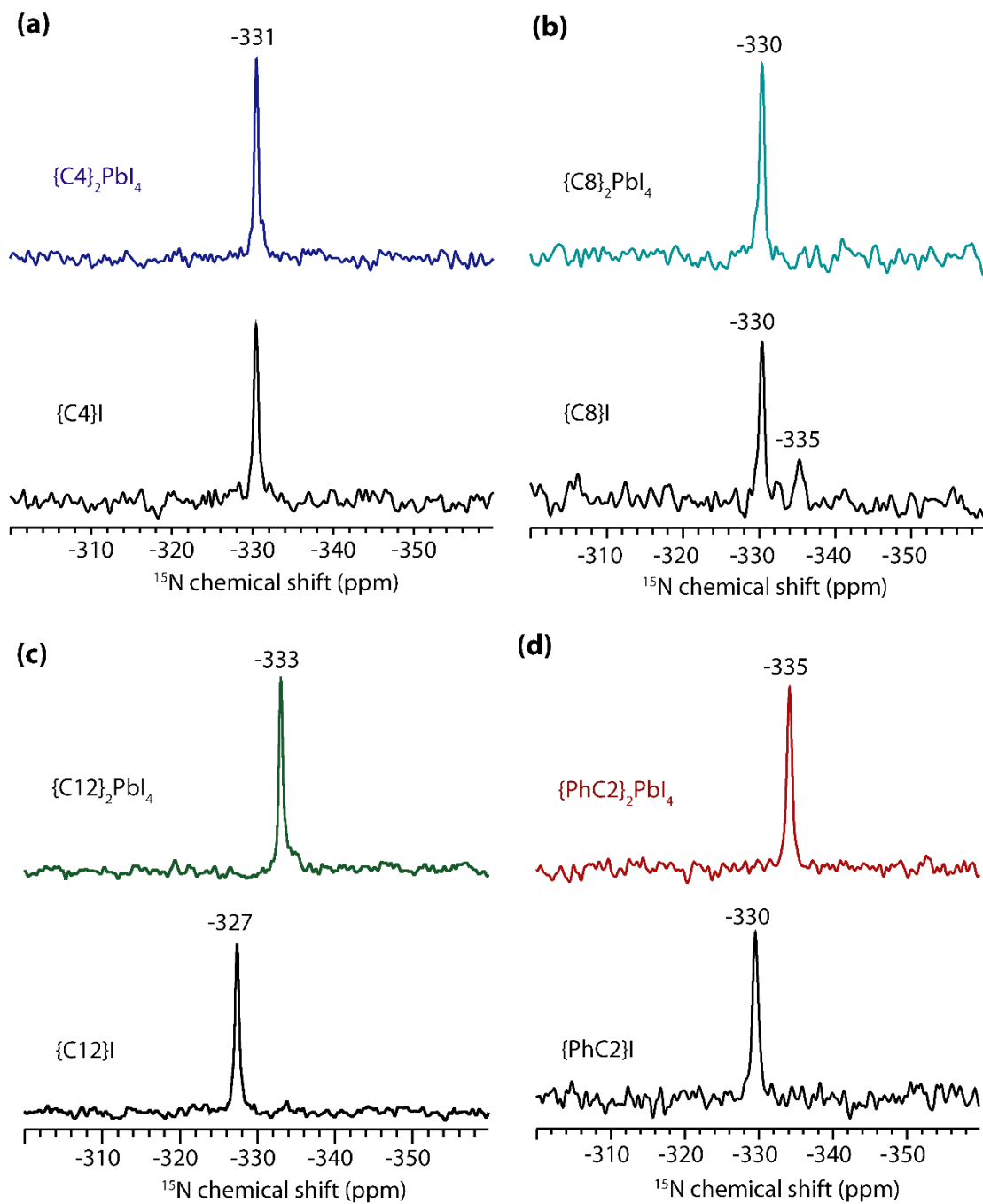


Figure S13. Solid-state 1D $^{15}\text{N}\{^1\text{H}\}$ CP-MAS NMR spectra of (a) $\{C4\}_2\text{PbI}_4$ and $\{C4\}\text{I}$, (b) $\{C8\}_2\text{PbI}_4$ and $\{C8\}\text{I}$, (c) $\{C12\}_2\text{PbI}_4$ and $\{C12\}\text{I}$, and (d) $\{\text{PhC}2\}_2\text{PbI}_4$ and $\{\text{PhC}2\}\text{I}$.

References

- (1) Kolodziejski, W.; Klinowski, J. Kinetics of Cross-Polarization in Solid-State NMR: A Guide for Chemists. *Chem. Rev.* **2002**, *102*, 613–628.
- (2) Pines, A.; Gibby, M. G.; Waugh, J. S. Proton-enhanced NMR of Dilute Spins in Solids. *J. Chem. Phys.* **1973**, *59*, 569–590.
- (3) Schanda, P.; Huber, M.; Boisbouvier, J.; Meier, B. H.; Ernst, M. Solid-State NMR Measurements of Asymmetric Dipolar Couplings Provide Insight into Protein Side-Chain Motion. *Angew. Chem. Int. Ed.* **2011**, *50*, 11005–11009.
- (4) Fülber, C.; Demco, D. E.; Blümich, B. The Influence of Molecular Motion on Cross-Polarization in Cross-Linked Elastomers. *Solid State Nucl. Magn. Reson.* **1996**, *6*, 213–223.
- (5) Ueda, T.; Shimizu, K.; Ohki, H.; Okuda, T. ¹³C CP/MAS NMR Study of the Layered Compounds [C₆H₅CH₂CH₂NH₃]₂[CH₃NH₃]_{n-1}Pb_nI_{3n+1} (n = 1, 2). *Z. Für Naturforschung A* **1996**, *51*, 910–914.
- (6) Ueda, T.; Omo, M.; Shimizu, K.; Ohki, H.; Okuda, T. Ionic Motion of Phenethylammonium Ion in [C₆H₅CH₂CH₂NH₃]₂PbX₄ (X = Cl, Br, I) as Studied by ¹H NMR. *Z. Für Naturforschung A* **1997**, *52*, 502–508.
- (7) Seyfarth, L.; Senker, J. An NMR Crystallographic Approach for the Determination of the Hydrogen Substructure of Nitrogen Bonded Protons. *Phys. Chem. Chem. Phys.* **2009**, *11*, 3522–3531.
- (8) Paluch, P.; Pawlak, T.; Amoureux, J.-P.; Potrzebowski, M. J. Simple and Accurate Determination of X–H Distances under Ultra-Fast MAS NMR. *J. Magn. Reson.* **2013**, *233*, 56–63.
- (9) Paluch, P.; Pawlak, T.; Ławniczak, K.; Trébosc, J.; Lafon, O.; Amoureux, J.-P.; Potrzebowski, M. J. Simple and Robust Study of Backbone Dynamics of Crystalline Proteins Employing ¹H–¹⁵N Dipolar Coupling Dispersion. *J. Phys. Chem. B* **2018**, *122*, 8146–8156.
- (10) Paluch, P.; Trébosc, J.; Amoureux, J.-P.; Potrzebowski, M. J. ¹H–³¹P CPVC NMR Method under Very Fast Magic Angle Spinning for Analysis of Dipolar Interactions and Dynamics Processes in the Crystalline Phosphonium Tetrafluoroborate Salts. *Solid State Nucl. Magn. Reson.* **2017**, *87*, 96–103.
- (11) Paluch, P.; Pawlak, T.; Jeziorna, A.; Trébosc, J.; Hou, G.; Vega, A. J.; Amoureux, J.-P.; Dracinsky, M.; Polenova, T.; Potrzebowski, M. J. Analysis of Local Molecular Motions of Aromatic Sidechains in Proteins by 2D and 3D Fast MAS NMR Spectroscopy and Quantum Mechanical Calculations. *Phys. Chem. Chem. Phys.* **2015**, *17*, 28789–28801.
- (12) Lemmerer, A.; Billing, D. G. Synthesis, Characterization and Phase Transitions of the Inorganic–Organic Layered Perovskite-Type Hybrids [(C_nH_{2n+1}NH₃)₂PbI₄], n = 7, 8, 9 and 10. *Dalton Trans.* **2012**, *41*, 1146–1157.
- (13) Billing, D. G.; Lemmerer, A. Synthesis, Characterization and Phase Transitions of the Inorganic–Organic Layered Perovskite-Type Hybrids [(C_nH_{2n+1}NH₃)₂PbI₄] (n = 12, 14, 16 and 18). *New J. Chem.* **2008**, *32*, 1736–1746.
- (14) Billing, D. G.; Lemmerer, A. Synthesis, Characterization and Phase Transitions in the Inorganic–Organic Layered Perovskite-Type Hybrids [(C_nH_{2n+1}NH₃)₂PbI₄], n = 4, 5 and 6. *Acta Crystallogr. Sect. B* **2007**, *63*, 735–747.

- (15) Straus, D. B.; Iotov, N.; Gau, M. R.; Zhao, Q.; Carroll, P. J.; Kagan, C. R. Longer Cations Increase Energetic Disorder in Excitonic 2D Hybrid Perovskites. *J. Phys. Chem. Lett.* **2019**, *10*, 1198–1205.
- (16) Aleksandrov, K. S.; Bartolomé, J. Structural Distortions in Families of Perovskite-like Crystals. *Phase Transit.* **2001**, *74*, 255–335.
- (17) Aleksandrov, K. S. Structural Phase Transitions in Layered Perovskitelike Crystals. *Crystallogr. Rep.* **1995**, *40*.
- (18) Glazer, A. M. The Classification of Tilted Octahedra in Perovskites. *Acta Crystallogr. B* **1972**, *28*, 3384–3392.